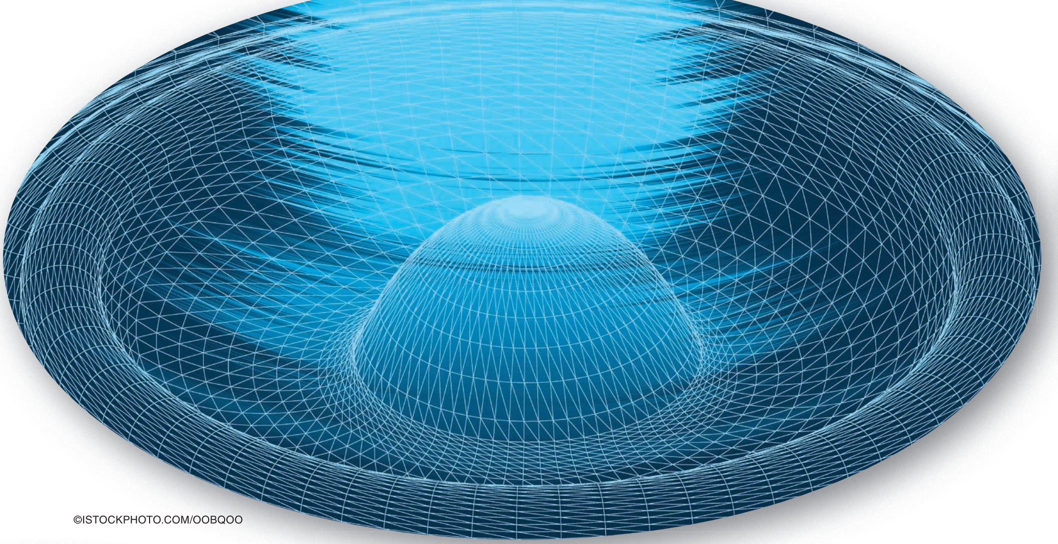

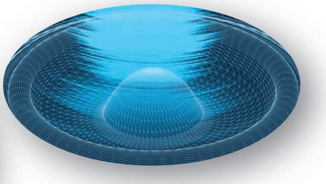

©ISTOCKPHOTO.COM/OOBQOO

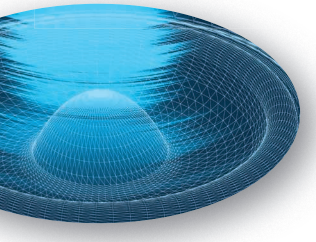

Imaging Acoustic Waves by Microwave Microscopy

Lu Zheng, Linbo Shao, Marko Loncar, and Keji Lai

Atoms in all materials are constantly shaking, which is largely responsible for the transfer of heat and sound. In a uniform crystalline solid, the motion of the lattice can be decomposed into just a handful of normal modes of vibration or, in the language of quantum mechanics, a set of quantized eigenmodes of the elastic structure known as *phonons* [1]. In the frequency (f) regime of interest for microwave engineers, there exist three (one longitudinal, two shear) branches of vibrational modes with long wavelengths—"long" when compared with the atomic spacing. Their frequencies, which represent the energy of each quantum,

Nomenclature Used Throughout

It should be noted that the term *elastic waves* is often used when the emphasis is on the classical description of solids as continuous elastic media. The term *acoustic waves*, on the other hand, emphasizes the linear dispersion relation in the long-wavelength limit. In this article, we continue to use *acoustic waves* for a natural connection to other rapidly evolving fields such as acousto-electronics and acousto-optics.

Lu Zheng (luzheng@utexas.edu) and Keji Lai (kejilai@physics.utexas.edu) are with the Department of Physics, University of Texas at Austin, United States. Linbo Shao (linboshao@g.harvard.edu) and Marko Loncar (loncar@seas.harvard.edu) are with the John A. Paulson School of Engineering and Applied Sciences, Harvard University, Cambridge, Massachusetts, United States.

Digital Object Identifier 10.1109/MMM.2020.3008240
Date of current version: 8 September 2020

Authorized licensed use limited to: Cornell University Library. Downloaded on September 08,2020 at 12:56:23 UTC from IEEE Xplore. Restrictions apply.

are linearly proportional to the inverse wavelengths, which represent the momentum of each quantum. The ratio between the two is typically several kilometers per second. In good crystals with few imperfections, these vibrations travel a very long distance—"long" when compared with the wavelength—with little decay of the amplitude under the ambient temperature and pressure. At audio frequencies, these sound waves can propagate in solids. They are commonly known as *acoustic waves* (see "Nomenclature Used Throughout").

The connection between acoustic waves and microwave electronics dates back to the 1950s, when scientists at Bell Labs demonstrated the generation and detection of longitudinal and shear waves at a few gigahertz in quartz crystals [2]. It was soon recognized that, because the speed of sound in solids is 10^5 times smaller than the speed of light, microwave acoustic devices using piezoelectric transducers [3] could afford substantial miniaturization in the system dimension. In particular, compact resonators that take advantage of the ultralow loss of bulk acoustic waves (BAWs) in quartz have found widespread application in professional electronic equipment [4]. Starting from the late 1960s, much attention was directed toward the guided waves along the free surface of materials [5], which were first explained by Lord Rayleigh in his seminal 1885 paper [6]. Named after the discoverer, Rayleigh waves, or surface acoustic waves (SAWs), have a lower speed than BAWs and low propagation loss. They are easily accessible from the surface and readily compatible with the planar technology developed for integrated semiconductor devices. To date, SAW devices, such as delay lines, filters, oscillators, transformers, and sensors, are indispensable in most microwave systems [7], [8] and will continue to thrive in the 5G era. It is anticipated that the global SAW market will reach a remarkable number of US$3.4 billion by the end of 2024 [9].

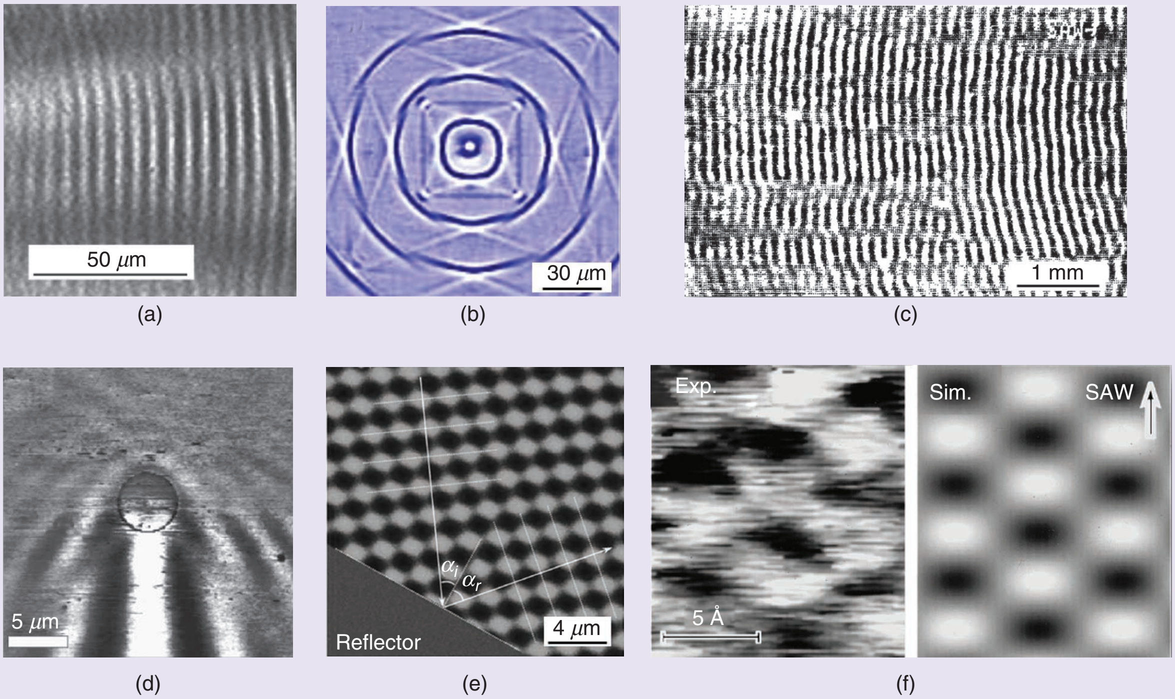

(a) (b) (c)

(d) (e) (f)

Figure 1. *(a) A stroboscopic X-ray topograph of traveling Rayleigh waves on gallium arsenide (GaAs) taken with the driving signal phase-locked to the synchrotron radiation emission [18]. The SAW is excited at 579 MHz. (Source: [18]; used with permission from the American Institute of Physics.) (b) A surface phonon image on the (001) TeO_2 surface taken by pump-probe scanning laser interferometry [21]. SAWs are thermoelastically excited by the 415-nm pump laser with a repetition rate of 80 MHz. (Source: [21]; used with permission from the American Physical Society.) (c) Scanning electron photographs of the traveling SAW on $LiNbO_3$ [24]. The excitation frequency is 25.127 MHz. (Source: [24]; used with permission from the American Institute of Physics.) (d) An SAFM amplitude image on the (001) GaAs [27]. A scattering dot [gold (Au), diameter 5 μm] is denoted by the black circle in the center. The SAW is excited at 694 MHz, and a nearby IDT (not shown) sends a slightly detuned signal for the SAFM imaging. (Source: [27]; used with permission from the American Institute of Physics.) (e) A dynamic EFM image of SAW interference near a metal reflector, showing both the incident and reflected wave fronts. The tip resonant frequency is ~ 75 kHz, and the SAW is excited at 1.585 GHz [32]. (f) A comparison between measured (left) and modeled (right) STM images of the Au (111) surface excited at 39.5 MHz and clocked at 39.51 MHz [36]. (Source: [36]; used with permission from the American Institute of Physics.) Exp.: experimental; Sim.: simulated.*

Authorized licensed use limited to: Cornell University Library. Downloaded on September 08,2020 at 12:56:23 UTC from IEEE Xplore. Restrictions apply.

The characteristic dimension of SAW devices using interdigital transducers (IDTs) is set by the acoustic wavelength in piezoelectric solids, which is typically a few micrometers at 1 GHz. In other words, the inherent length scale to observe wave phenomena, such as interference, diffraction, and localization of SAWs, is in the mesoscopic regime. High-resolution imaging of the acoustic displacement field or the accompanying electric field is therefore highly desirable for designing, characterizing, and ultimately improving SAW devices [7]. Moreover, it has been shown that, in artificial structures with periodic piezoelectric properties, the coupling between gigahertz electromagnetic waves (photons) and acoustic waves (phonons) can lead to polaritons with different phononic bands [10]–[15]. Spatial mapping of the SAW fields, in conjunction with numerical simulations of the phononic metamaterials, is thus of great interest to advance this research field.

In the past few decades, microscopy techniques have evolved rapidly to provide various means for visualizing gigahertz acoustic waves. Figure 1(a) shows an image of surface waves taken by stroboscopic X-ray topography [18]. Here the "strobe" is obtained by a phase lock between the X-ray source and the excitation of the SAW device, resulting in a stationary image of the propagating surface wave [16]–[18]. A major drawback of the technique is the need for coherent X-rays from a synchrotron radiation light source, which limits its widespread use in the laboratory scale. A somewhat related technique that also utilizes light to visualize acoustic displacement is scanning laser reflectometry [19], [20] or interferometry [21]–[23]. The technique can resolve subpicometer out-of-plane displacement with subnanosecond temporal resolution, as exemplified by the beautiful snapshot of the propagating wave on the (001) tellurium dioxide (TeO_2) surface [21] in Figure 1(b). The lateral spatial resolution, however, is diffraction-limited to $\sim 1\ \mu m$ due to the use of the visible laser. In the early 1990s, it was also demonstrated that the secondary electrons in a scanning electron microscope (SEM) could be modulated by the SAW electric field, forming a stationary pattern of the propagating wave [24]–[26] [Figure 1(c)]. The applicability of this method, however, is rather limited due to the strong charging effect in insulating piezoelectric crystals, resulting in a moderate resolution of about $1\ \mu m$ and an operation frequency below 0.5 GHz.

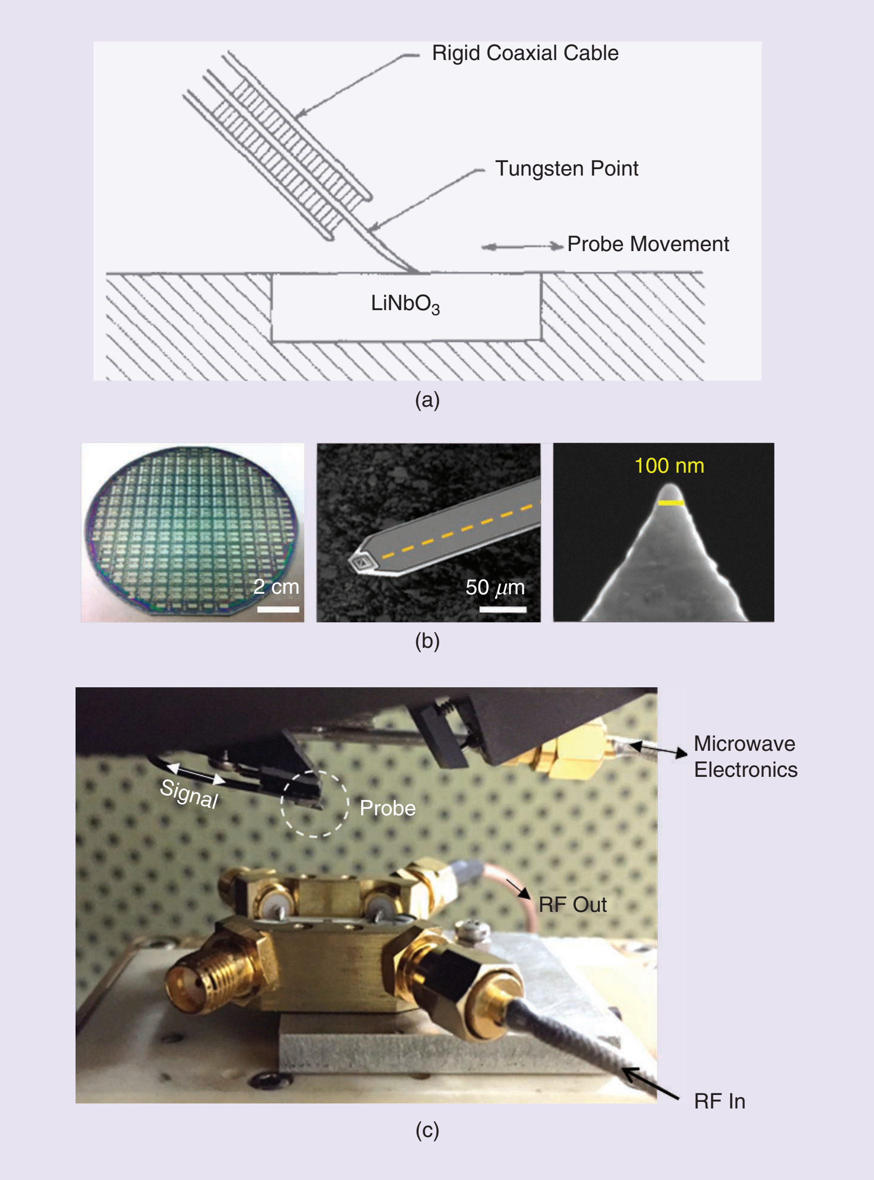

Figure 2. *(a) The experimental setup of an early attempt to probe the SAW electric field. (Source: [37]; used with permission from the American Institute of Physics.) (b) From left to right: batch-fabricated probes on a four-inch wafer; cantilever with metallic shield and buried center conductor (orange dashed line); close-up view of the tip apex. (Source: [38]; used with permission from IOP Publishing.) (c) The AFM-based setup for imaging SAW devices with RF connections.*

Authorized licensed use limited to: Cornell University Library. Downloaded on September 08,2020 at 12:56:23 UTC from IEEE Xplore. Restrictions apply.

The advent of scanning probe microscopy has brought in a new impetus to image SAWs with nanoscale spatial resolution. In a typical atomic force microscopy (AFM) setup, the mechanical resonance of the cantilever of several hundred kilohertz is far below the microwave regime. As a result, scanning acoustic force microscopy (SAFM) works in a heterodyne scheme [27]–[31] that mixes the acoustic sample wave with a slightly detuned reference wave from another source. This leads to cantilever oscillations at a difference frequency being measured by conventional photodiode detection [Figure 1(d)]. Similarly, by mixing a signal at the mechanical resonance of the probe and a second component at microwave frequency, dynamic electrostatic force microscopy (EFM) can measure the cantilever deflection due to the piezoelectric polarization field. Figure 1(e) shows such an EFM image of the interference pattern arising from a metal reflector on a SAW device [32]. Finally, the surface oscillation excited by propagating SAWs can be imaged by stroboscopic scanning tunneling microscopy (STM) [33]–[36], as shown in Figure 1(f). Interested readers are referred to the review article by Hesjedal [31] for a comprehensive overview of these techniques.

Despite some success of SAFM/EFM/STM to image the SAW displacement field, the spatial distribution of the SAW electric field, which is of paramount importance for electronic applications, has not been thoroughly studied. In an early attempt to map out the piezoelectric surface potential [Figure 2(a)], a tungsten tip at the end of a coaxial cable raster scanned on lithium niobate ($LiNbO_3$) and the detected SAW signal were demodulated by a microwave analyzer [37]. While this simple configuration did capture the basic idea, it is clear that much more engineering effort is needed to perform nanoscale SAW imaging. The modern version of the probe [Figure 2(b)] consists of wafer-scale microfabricated cantilever tips with electrical shielding and a sub-100-nm tip apex [38]. These probes are commercially available from PrimeNano Inc. Figure 2(c) shows a close-up view of the experimental apparatus, where microwave signals are fed to both the tip and the SAW device. The AFM platform provides the necessary topographic feedback for high-resolution imaging work.

Microwave Impedance Microscopy

The schematic of a typical microwave microscope is depicted in Figure 3(a). In this mode of operation, the microwave signal is delivered to the center conductor of the tip through an impedance-match (Z-match) section. The reflected signal is amplified and demodulated by an in-phase/quadrature (IQ) mixer. As seen from the equivalent circuit in Figure 3(b), the microwave electronics detect the small variation of tip-sample impedance $Z_{t\text{–}s}$ during the raster scan, thus the term *microwave impedance microscopy* (*MIM*) [39], [40]. By adjusting the local oscillator (LO) phase ϕ, the real and imaginary components of the admittance change $\Delta Y_{t\text{–}s} = (Z_{t\text{–}s})^{-1}$ can be mapped as MIM-Real (MIM-Re) and MIM-Imaginary (MIM-Im) images, respectively. It should be noted that most works on microwave microscopy in the literature (although with different acronyms) are based on the same underlying physics. The reflection-mode MIM (RMIM) is widely used to study nanoscale permittivity and conductivity distribution in advanced materials, as surveyed by other articles in

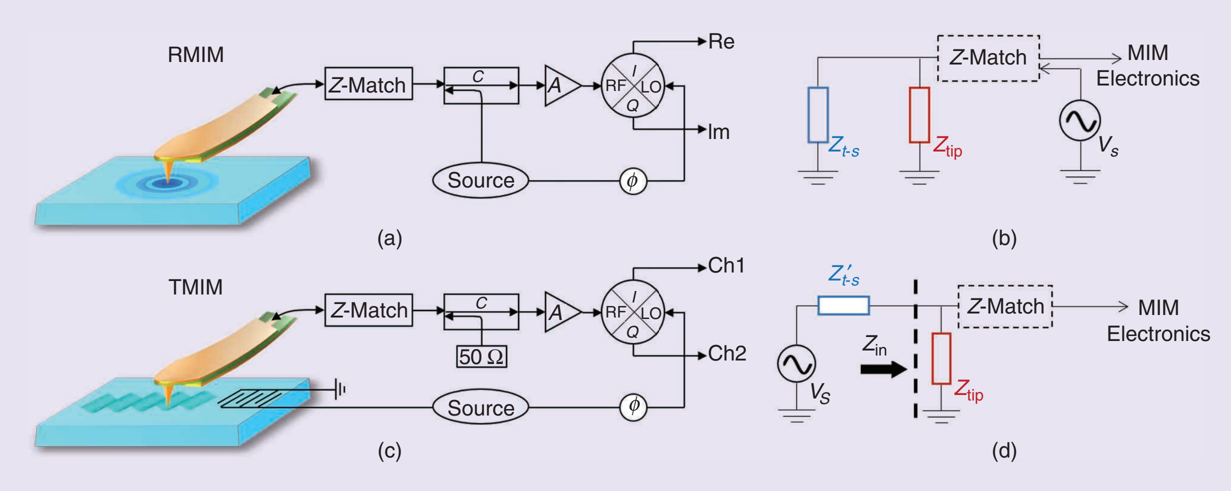

Figure 3. *(a) The schematic of the RMIM [39], [40]. The excitation signal is delivered to the tip, and the reflected signal is amplified and demodulated by the IQ mixer to form the RMIM-Re and RMIM-Im images. (b) The equivalent circuit of the RMIM. (c) The schematic of the TMIM [41]. The excitation signal is delivered to the IDT on the sample, and the transmitted signal is amplified and demodulated by the IQ mixer to form the TMIM-Ch1 and TMIM-Ch2 images. (d) The equivalent circuit of the TMIM. (Source: [41]; used with permission from the American Physical Society.) C: coupler; A: amplifier; ϕ: phase shifter.*

Authorized licensed use limited to: Cornell University Library. Downloaded on September 08,2020 at 12:56:23 UTC from IEEE Xplore. Restrictions apply.

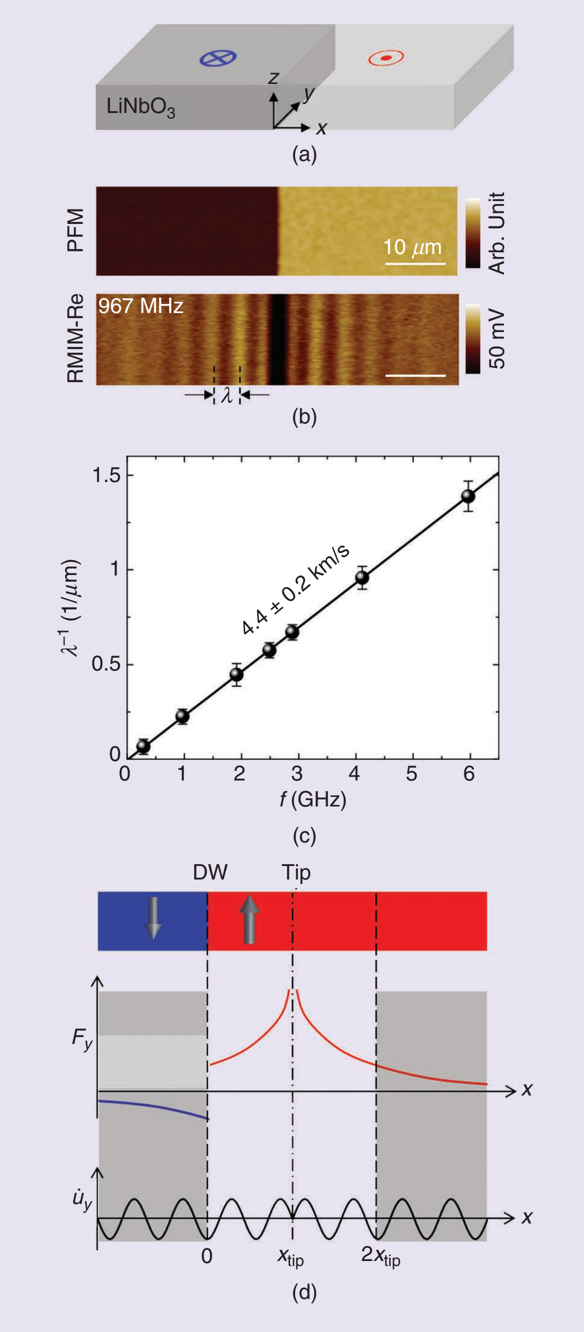

Figure 4. *(a) The schematic of the z-cut $LiNbO_3$ sample with a single DW. (b) The PFM phase (top) and RMIM-Re (bottom) images of the sample [51]. The spacing of the bright fringes is labeled λ. The scale bars are 10 µm. (c) The linear relation between λ^{-1} and the RMIM frequency. The slope corresponds to a wave velocity of 4.4 ± 0.2 km/s. (d) Top: The schematic view of the tip–sample configuration in the xz-plane. Middle: A sketch of the y-component of the electromechanical force. Bottom: The time derivative of the displacement field near the surface. The sign of F_y is flipped in opposite domains. The overlap integral of $F_y \cdot \dot{u}_y$ in the two shaded areas leads them to cancel each other. (Source: [51]; used with permission from the United States National Academy of Sciences). Arb.: arbitrary.*

this special issue. We show later that the technique can also offer insights regarding piezoelectric transduction in ferroelectric materials.

The RMIM can be easily reconfigured in the transmission-mode MIM (TMIM) to perform direct imaging of SAW electric fields [41]. As illustrated in Figure 3(c), the microwave signal is delivered to the IDT on a piezoelectric sample, and the tip acts as a movable receiver. The oscillating SAW field coupled to the tip is then demodulated as two orthogonal output channels, TMIM-Ch1 and TMIM-Ch2. The equivalent circuit of the TMIM configuration is shown in Figure 3(d). The time-varying source potential V_s is picked up by the tip, followed by the same amplification and demodulation in the microwave electronics. Specifically, the input signal to the TMIM tip is given by

$$V_{\text{in}} = V_s \cdot Z_{\text{in}} / (Z'_{t-s} + Z_{\text{in}}) \approx V_s \cdot Z_{\text{in}} / Z'_{t-s}, \qquad (1)$$

where $|Z_{\text{in}}| \sim 1\ \text{K}\Omega$ is the effective input impedance of the tip/Z-match section at the receiver and $|Z'_{t-s}| \sim 100\ \text{K}\Omega$ is the tip-sample coupling impedance [41]. It should be noted that similar transmission-type probes have been used to map out the RF fields in microwave resonators [42], [43] and metamaterials [44], [45]. In those systems, however, the characteristic length scale is set by the electromagnetic rather than the acoustic wavelength, and the mesoscopic resolution is not necessary.

Before discussing the experimental results, we would like to point out that, in conventional microwave microscopy where the electrical property is of interest, RMIM and TMIM provide similar information on the local variation of permittivity or conductivity. In the presence of a piezoelectric transducer that launches a propagating SAW, however, the two may yield rather different information of the sample, which will be elaborated in the section that follows.

RMIM Results

Most microwave imaging of SAWs to date has been carried out on $LiNbO_3$, an important acousto-electronic and acousto-optic material for its high piezoelectric constant [46], low acoustic attenuation [47], [48], and strong nonlinear optical coefficients [49], [50]. $LiNbO_3$ has a trigonal (class 3 m) crystal structure with a mirror *yz* plane and a direct triad *z*-axis along the polar direction [46]. It is a ferroelectric material, and the spontaneous polarization can be switched by electrical poling [49]. Figure 4(a) shows the simplest scenario involving a lithographically defined straight domain wall (DW) on a *z*-cut $LiNbO_3$ sample [51]. The two oppositely polarized domains are seen in the piezo-force microscopy (PFM) image in Figure 4(b). The RMIM-Re image taken at $f = 967$ MHz, on the other hand, exhibits clear interference fringes around the DW. Because the electrical conductance of the insulating $LiNbO_3$ is negligible, the

Authorized licensed use limited to: Cornell University Library. Downloaded on September 08,2020 at 12:56:23 UTC from IEEE Xplore. Restrictions apply.

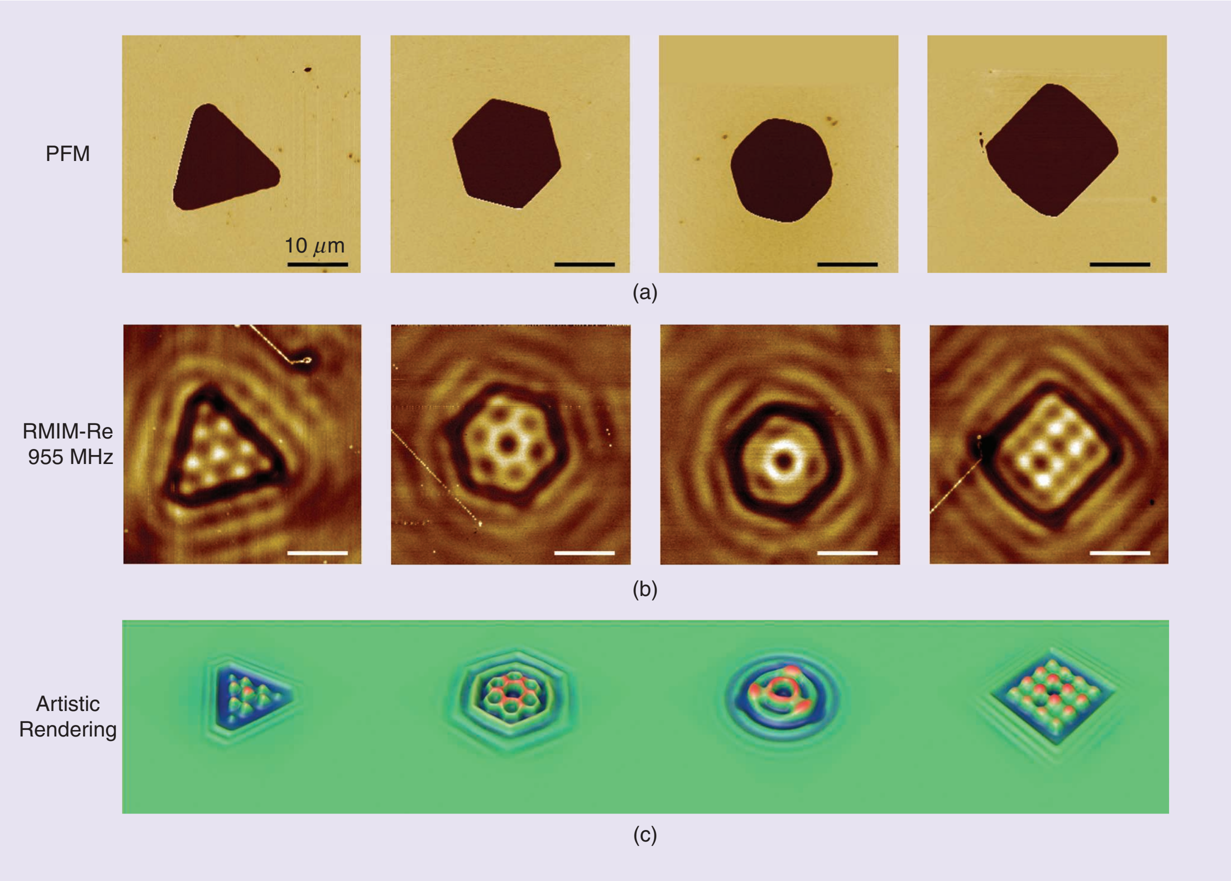

Figure 5. *(a) PFM and (b) RMIM-Re images at $f = 955$ MHz of four closed LiNbO$_3$ domains. Interference patterns due to the superposition of ripples around each DW are seen in the microwave data. Scale bars are 10 μm. (c) An artistic rendering of the corresponding microwave images. (Source: [51]; used with permission from the United States National Academy of Sciences.)*

RMIM-Re contrast clearly indicates that the microwave energy is dissipated through the piezoelectric transduction rather than through the Ohmic loss.

The main features of the microwave image include a prominent dip at the DW and damped oscillations with a periodicity of 4.5 μm away from the wall. It is certainly tempting to interpret these fringes as the standing-wave pattern of the acoustic displacement field underneath the tip [52]. However, should this be the case, the measured periodicity would indicate the dominance of a guided wave with an unphysically large phase velocity of 8.8 km/s. In fact, since the acoustic impedance is the same for both domains, the reflection of the displacement fields from the *yz* DW should be rather weak for acoustic waves. The RMIM-Re interference pattern in Figure 4(b) is therefore nontrivial and calls for a careful analysis of the tip-sample interaction.

As shown in Figure 4(c), the measured $1/\lambda$ (λ being the period of the RMIM-Re fringes) scales with the microwave frequency from 285 MHz to 6 GHz. The slope of 4.4 ± 0.2 km/s closely matches that of the pseudo-SAW (P-SAW) [53], [54], which exists only on the surface of piezoelectric materials. The dispersion of this surface wave lies in the continuum of bulk waves, and its energy leaks into the bulk during the propagation [54]. Unlike the Rayleigh SAW, the displacement field of this Bleustein–Gulyaev-like SAW [55], [56] is primarily polarized in the *y*-direction [57], although the wave is not purely transverse-horizontal due to the lack of an even-order symmetry axis in LiNbO$_3$.

Given the preceding background information, the RMIM result can be understood as follows. In LiNbO$_3$, the local mechanical strain and electric field are coupled by the third-rank piezoelectric tensors, whose signs are flipped across opposite domains [46]. The RMIM-Re measures the loss in electrical power, which by energy conservation equals the gain in mechanical power of various acoustic waves in solids. Since the P-SAW is dominated by the *y*-component of its displacement fields [57], the power transduction is predominantly determined by the overlap between F_y and $\dot{u}_y$, the *y*-components of the electromechanical force density and time derivative of the displacement, respectively. As seen in Figure 4(d), F_y flips sign in different domains, whereas $\dot{u}_y$ is an even function with respect to the tip position. The overlap integral in the two shaded areas results in the two canceling each other,

Authorized licensed use limited to: Cornell University Library. Downloaded on September 08,2020 at 12:56:23 UTC from IEEE Xplore. Restrictions apply.

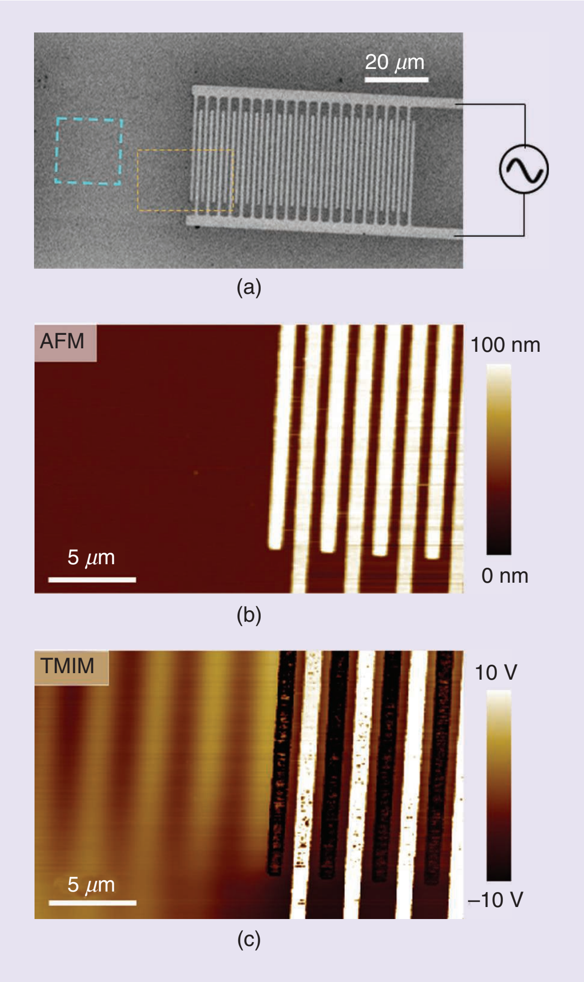

(a)

(b)

(c)

Figure 6. *(a) The SEM image of the SAW device. The (b) AFM and (c) TMIM images in the dashed orange rectangle in (a). Wavelike features are seen in the TMIM data. (Source: [41]; used with permission from the American Physical Society.)*

leading to a drop in power transduction when the tip is close to the wall. As the tip moves away from the DW, the truncated overlap integral oscillates with one-wavelength periodicity and shows the damping in amplitude. Note that the analysis here provides only a qualitative physical picture. For a more in-depth discussion, readers are referred to [51] for the full numerical simulation of the acoustic fields and power transduction.

The interference of piezoelectric transduction can be further appreciated in the $LiNbO_3$ coral domains formed by electrical poling [51]. Figure 5(a) and (b) shows the PFM and RMIM-Re images of four closed domains shaped in an equilateral triangle, a hexagon, a circle, and a square, respectively. Because of the crystal symmetry, straight DWs on the *z*-cut $LiNbO_3$ surface can form only along the three *y*-equivalent axes. Consequently, the domain designed to be a circle appears as a rounded hexagon, and the domain designed to be a square appears as a distorted rectangle. Beautiful interference patterns due to the superposition of ripples around each DW are observed in the microwave images. At first sight, these visually attractive features [artistic rendering in Figure 5(c)] are reminiscent of the electron waves in quantum corals imaged by STM [58]. In stark contrast to those standing-wave patterns, however, the adjacent nodes in the RMIM data are not spaced by a half wavelength. The existence of such patterns does not indicate the presence of acoustic resonance. In other words, the bright and dark regions in the RMIM-Re images mark the tip locations around which the piezoelectric transduction is highly effective and ineffective, respectively.

Putting these findings in perspective, the RMIM experiment reveals some internal degrees of freedom in piezoelectric and elastic tensors, which are not accessible by measurements of the acoustic displacement fields. On the other hand, the microwave electric field from the tip can excite many modes of acoustic waves in piezoelectrics, which may complicate image analysis. For the purpose of SAW imaging, the TMIM detection of waves generated by external sources (as reviewed in the next section) would be preferable.

TMIM Results

Figure 6(a) shows the SEM image of an IDT designed to excite the *x*-propagating Rayleigh-type SAW on a *z*-cut $LiNbO_3$ crystal, which was poled to be a single ferroelectric domain prior to device fabrication. Figure 6(b) and (c) displays the simultaneously acquired AFM and TMIM images when the IDT was powered by a 10-dBm microwave at $f = 957$ MHz [41]. While only the interdigital fingers are seen in the surface topography, the electrical potential sharing a spatial periodicity consistent with the Rayleigh SAW ($v = 3.8$ km/s) [48] can be clearly imaged by TMIM. Here the tip picks up an input signal proportional to the SAW potential. Signals at the RF and LO ports of the mixer can be represented as $V_{\mathrm{RF}} \propto V_s \propto e^{i(\omega t - kx)}$ and $V_{\mathrm{LO}} \propto e^{i(\omega t + \phi)}$, respectively, where ω represents the angular frequency, k the acoustic wave vector, and ϕ the mixer phase. Ignoring the terms containing $2\omega t$, one can see that the system demodulates the time-varying SAW potential into time-independent spatial patterns, as observed in the TMIM data.

We now turn to the TMIM imaging of a standing wave formed by two counterpropagating SAWs. Figure 7(a) shows the schematic of the experimental setup, where two balanced signals (0 dBm in amplitude) with a phase offset of θ are fed into a pair of IDTs. This geometry is technologically important in that it can create acoustic trapping potentials for electrons. Following the same analysis as previously, the input signals to the mixer can be written as $V_{\mathrm{RF}} \propto e^{i(\omega t - kx)} + e^{i(\omega t + kx + \theta)}$ and $V_{\mathrm{LO}} \propto e^{i\omega t}$. The LO phase ϕ is omitted since it

Authorized licensed use limited to: Cornell University Library. Downloaded on September 08,2020 at 12:56:23 UTC from IEEE Xplore. Restrictions apply.

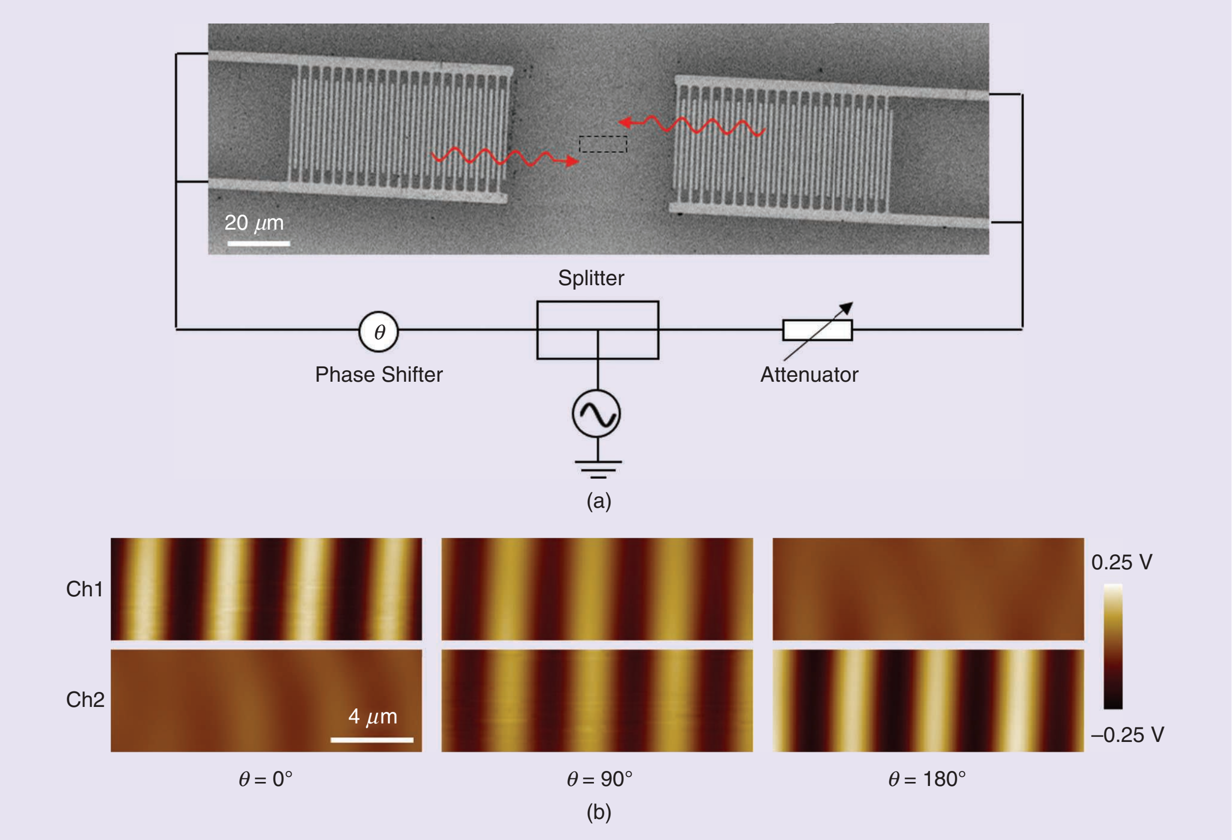

Figure 7. *(a) The schematic diagram for the imaging of counter-propagating waves. Two signals (0 dBm in amplitude and phase offset by θ) split from the same source are fed into the two IDTs. (b) TMIM images at different values of θ showing the transition of signal strength from Ch1 to Ch2. (Source: [41]; used with permission from the American Physical Society.)*

contributes the same phase to both channels. The mixer then generates two output signals as follows:

$$V_{\mathrm{Ch1}} \propto \mathrm{Re}(V_{\mathrm{RF}} V_{\mathrm{LO}}^{*}) = \cos kx + \cos(kx+\theta), \tag{2}$$

$$V_{\mathrm{Ch2}} \propto \mathrm{Im}(V_{\mathrm{RF}} V_{\mathrm{LO}}^{*}) = -\sin kx + \sin(kx+\theta). \tag{3}$$

By tuning the phase difference θ between the two counterpropagating SAWs, the signal levels of the two TMIM channels can be varied. When $\theta = 0°$, the sinusoidal spatial patterns are expected to appear only in Ch1 ($V_{\mathrm{Ch1}} \propto 2\cos kx, V_{\mathrm{Ch2}} \propto 0$). The patterns should then be the same in both channels when $\theta = 90°$ ($V_{\mathrm{Ch1}} = V_{\mathrm{Ch2}} \propto \cos kx - \sin kx$) and completely move to Ch2 when $\theta = 180°$ ($V_{\mathrm{Ch1}} \propto 0, V_{\mathrm{Ch2}} \propto -2\sin kx$). As seen in Figure 7(b), the predicted evolution is again in excellent agreement with the measured TMIM data. The results demonstrate that TMIM can image the interference of acoustic waves in piezoelectric materials.

The nanoscale resolution of TMIM also enables the observation of wave diffraction. $\mathrm{LiNbO_3}$ wafers poled to be a single ferroelectric domain are energetically unstable. Over an extended period, small domains with opposite polarization may spontaneously form to reduce the electrostatic energy. As discussed in the previous section, the domain inversion flips the sign of odd-rank tensors (polarization, first rank; piezoelectric tensor, third rank), while leaving the even-rank tensors (permittivity, second rank; elasticity tensor, fourth rank) unchanged [46]. Since the acoustic impedance mostly depends on the density and elasticity of the material, the SAW displacement field is not strongly affected by the domain structure. In contrast, the SAW electric field, which is the gradient of the SAW potential, changes sign across a DW due to the piezoelectric coupling. In this sample, a small domain with spontaneous polarization reversal is found near the left IDT (the [AFM image in Figure 8(a)], as seen in the PFM image in Figure 8(b). Since its dimension is comparable to the acoustic wavelength, wave diffraction is expected around the domain. In Figure 8(c), the TMIM surface potential map indeed displays very strong distortion of the wavefront in this region. It is also important to note that the RMIM image [Figure 8(d)] taken in the same region and at the same frequency exhibits only weak interference rings as discussed previously, indicative of the different contrast mechanisms between the two modes of MIM.

The capability to resolve the spatial distribution of SAW potential is of particular interest for integrated

Authorized licensed use limited to: Cornell University Library. Downloaded on September 08,2020 at 12:56:23 UTC from IEEE Xplore. Restrictions apply.

phononic systems. For instance, when designing SAW resonators [20], [59], [60], which feature stronger electrical coupling and better confinement than their micromechanical counterparts, it is desirable to directly compare the simulated and measured spatial distribution of energy intensity of each acoustic cavity mode. In a recent report, a high-Q and small-mode-size SAW resonator on $LiNbO_3$ was demonstrated by engineering phononic band structures using adiabatically tapered structures [61]. As shown in Figure 9(a), the resonator consists of tapered couplers to enhance coupling to the source, phononic crystal sections to confine the phononic modes, and the resonant cavity. Compared to conventional Fabry–Perot resonators [20] that employ unperturbed free surfaces at the center and Bragg mirrors on the sides, the tapered grooves adiabatically change the reflectivity, resulting in a significantly reduced scattering loss of acoustic waves into the bulk and better confinement of phonons.

The SAW resonator device was designed to have two high-Q modes; these are indeed observed in the S_{21} spectra measured by a vector network analyzer [Figure 9(b)]. The period of the central cavity part is fine-tuned to align the resonant frequency of the fundamental mode to the center of the phononic crystal bandgap. Figure 9(c) displays the simulated energy density profiles of the fundamental (Mode 1) and second-order (Mode 2) modes of the SAW resonator. As shown in Figure 9(d), the single antinode in the middle of the resonator in Mode 1 and dual antinodes in Mode 2 are vividly seen in the SAW potential map measured by the TMIM [61]. The high quality of these modes can be further confirmed by taking TMIM data near the resonant frequency, as depicted in Figure 9(e). The substantial fall-off of the TMIM signal strength within 1 MHz around $f = 1.0384$ GHz provides direct evidence of the high Q factor (~ 10,000) of the second-order mode. We emphasize that, while the simulation and S_{21} measurement demonstrate the basic function, the spatially resolved TMIM images offer much more information on each section of the device. In-depth analysis of the local SAW images may reveal the effect of fabrication imperfections, crystal defects, and scattering from other phonons, which will provide insights for further improvement of device performance.

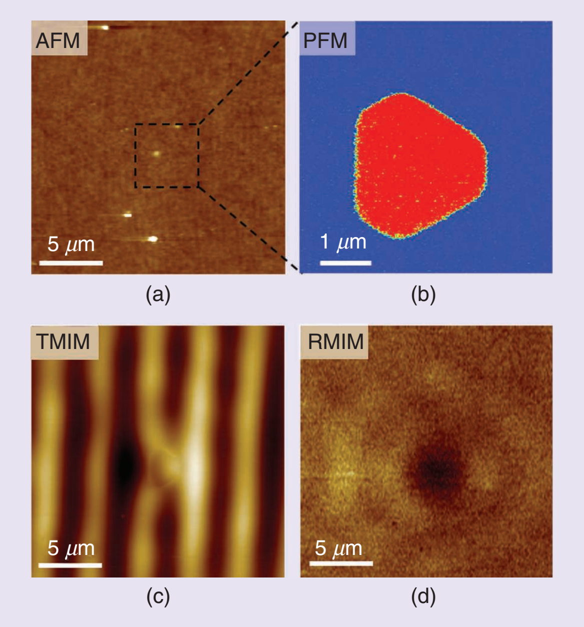

Figure 8. *(a) An AFM image in an area [the blue dashed square in Figure 6(a)] with a spontaneously reversed domain. (b) A close-up view of the PFM phase image inside the dashed square of (a). (c) TMIM and (d) RMIM images in the same area. (Source: [41]; used with permission from the American Physical Society.)*

Outlook

Compared with the widespread applications of near-field microwave microscopy in condensed matter physics, material science, device engineering, and biological research (covered by other topics in this special issue), the journey of microwave imaging on acoustic properties has just begun. In contrast to synchrotron-based, stroboscopic X-ray topography [16]–[18] and highly specialized scanning laser interferometry [21]–[23], the compatibility with tabletop AFM platforms makes the MIM a handy tool for individual laboratories. The nanoscale spatial resolution and accessibility to high-GHz microwaves are also desirable for next-generation SAW devices with higher operation frequencies.

The reflection-mode MIM has now developed into an important scientific instrument for the study of local dielectric constant [62], dielectric loss [63], and electronic conductivity [64]. In piezoelectrics, the results reviewed here highlight a new contrast mechanism due to electromechanical energy transduction. When imaging multidomain ferroelectric samples, it is imperative to include the contribution of acoustic waves in the data interpretation. Conversely, careful analysis of the RMIM results on novel multiferroics may uncover the intimate coupling of electric and strain/stress fields in these systems. The study may open a research frontier to explore various nanoscale elastic phenomena in these systems by electromagnetic imaging.

The TMIM is clearly advantageous for the imaging of the SAW electric field in various devices, such as delay lines, filters, and oscillators. While the demonstration described previously was performed in $LiNbO_3$, it is straightforward to expand the study to other popular acoustic materials, such as quartz, aluminum nitride, GaAs, and zinc oxide. More importantly, SAWs at the frequency of 1–10 GHz have attracted great interest in quantum science and engineering as an efficient means to couple superconducting qubits [65]–[67], drive spin

Authorized licensed use limited to: Cornell University Library. Downloaded on September 08,2020 at 12:56:23 UTC from IEEE Xplore. Restrictions apply.

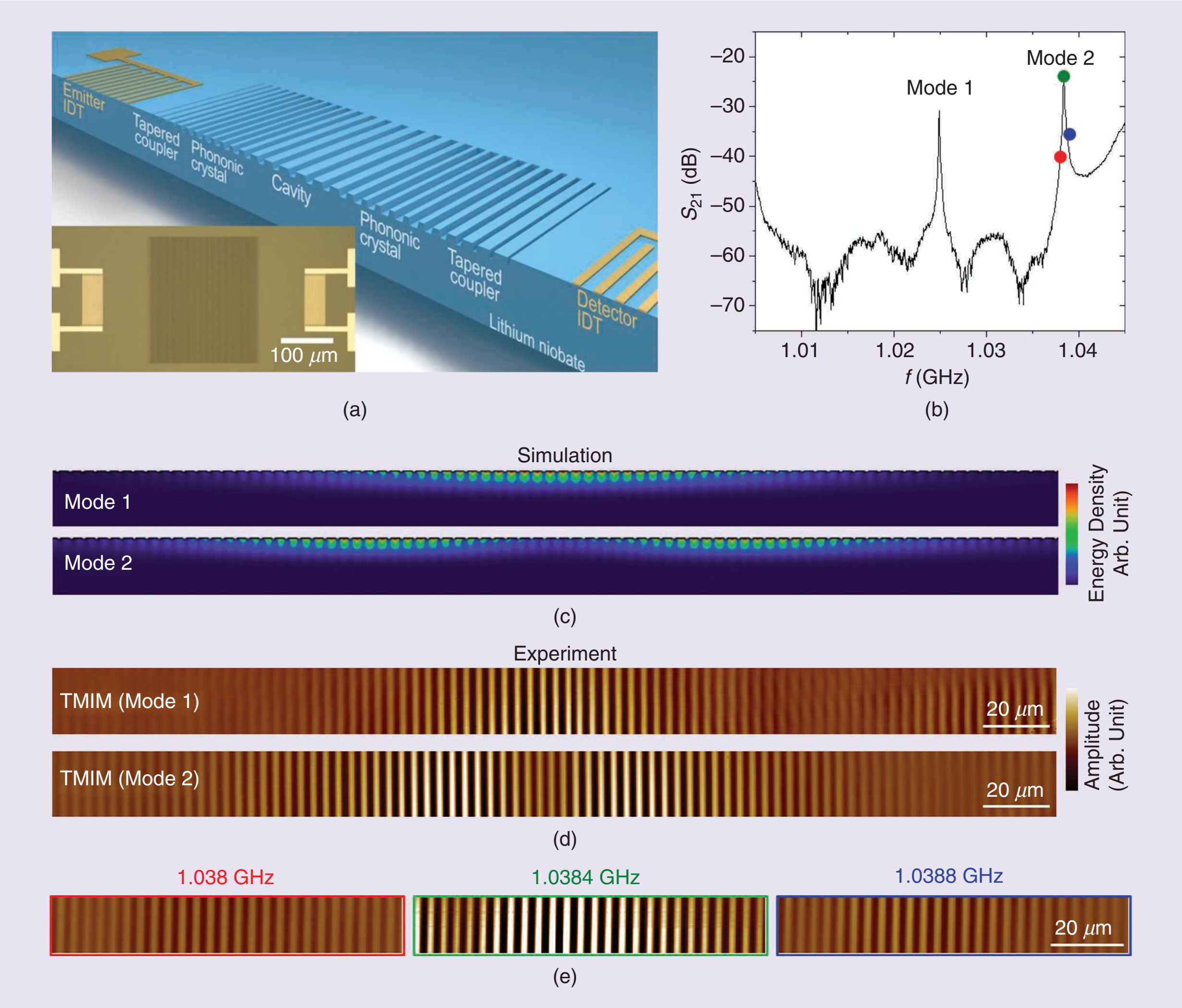

Figure 9. *(a) An illustration of the SAW resonator on LiNbO*$_3$*. The inset shows the optical microscope image of the fabricated device. The dark region at the center is the etched grooves and the bright regions on the sides are metal IDTs. (b) The transmission spectrum of a SAW resonator, showing the two high-Q modes in the bandgap of the phononic crystal. Note that the data are slightly different from those in [61] due to the use of a different device. (c) The mode profiles of the fundamental and second-order modes of the SAW resonator. The color scale indicates the total energy density of electromagnetic, kinetic, and elastic energy densities. (d) TMIM images of the measured SAW potential distribution at both modes [61]. (e) TMIM images at three different frequencies. The scanned area is centered at the right antinode of Mode 2. Color coding of the borders here matches that of the dots in (b). (Source: [61]; used with permission from the American Physical Society.)*

qubits [68]–[70], manipulate photons [71]–[73], and control 2D electrons [74]–[76]. Direct visualization of the SAW potential in different platforms will help with the understanding of quantum entanglement, quantum hybrid networks, and the deterministic teleportation of electrons. At the time of this writing, we are actively engaged along this line of research and a number of publications are forthcoming [77], [78].

Another potentially fruitful area for TMIM is 2D piezoelectric phononic crystals [13], [15], which are artificial structures formed through periodic spatial modulation of the elastic impedance. Through phonon–polariton coupling between electromagnetic waves and acoustic phonons, it is possible to form a complete bandgap that phonons cannot propagate in all directions [15]. The spatial distribution of acoustic fields inside the 2D structures, which at present is obtainable only by numerical simulation, is crucial to advance this branch of research. Moreover, through band structure engineering, one may even realize topological phononic crystals with robust edge channels [79]. The topological protection against acoustic defects will be vividly demonstrated by TMIM imaging. Interestingly, a major research direction of the RMIM is to investigate the electronic topological edges in quantum Hall [80] and quantum spin Hall [81] systems, as reviewed by Rubin et al. in this issue. In that

Authorized licensed use limited to: Cornell University Library. Downloaded on September 08,2020 at 12:56:23 UTC from IEEE Xplore. Restrictions apply.

sense, MIM may be the technique of choice to visualize topological boundary states in both real materials and metamaterials.

In summary, the research of near-field microwave microscopy has in the past few years expanded to the realm of acoustic waves. It is now possible to probe acousto-electronic behaviors in SAW devices, quantum materials, and phononic crystals with nanoscale spatial resolution. With continuous effort in this direction, we anticipate that exciting microwave microscopy works on acoustic waves will take place in the next few years.

References

[1] C. Kittel, *Introduction to Solid State Physics*, 8th ed. Hoboken, NJ: Wiley, 2005.

[2] H. E. Bommel and K. Dransfeld, "Excitation of very high frequency sound in quartz," *Phys. Rev. Lett.*, vol. 1, no. 7, p. 234, 1958. doi: 10.1103/PhysRevLett.1.234.

[3] E. H. Jacobsen, "Piezoelectric production of microwave phonons," *Phys. Rev. Lett.*, vol. 2, no. 6, p. 249, 1959. doi: 10.1103/PhysRevLett.2.249.

[4] V. E. Bottom, "A history of the quartz crystal industry in the USA," in *Proc. 35th Frequency Control Symp. IEEE*, 1981, pp. 3–21.

[5] R. M. White and F. W. Voltmer, "Direct piezoelectric coupling to surface elastic waves," *Appl. Phys. Lett.*, vol. 7, no. 12, p. 314, 1965. doi: 10.1063/1.1754276.

[6] L. Rayleigh, "On waves propagated along the plane surface of an elastic solid," *Proc. London Math. Soc.*, vol. s1–17, no. 1, pp. 4–11, 1885. doi: 10.1112/plms/s1-17.1.4.

[7] K-y. Hashimoto, *Surface Acoustic Wave Devices in Telecommunications–Modeling and Simulation*. Berlin: Springer-Verlag, 2000.

[8] R. Weigel et al., "Microwave acoustic materials, devices, and applications," *IEEE Trans. Microw. Theory Techn.*, vol. 50, no. 3, pp. 738–749, 2002. doi: 10.1109/22.989958.

[9] "SAW device market to grow US$ 3.4 billion by 2024," everythingRF, Apr. 12, 2019. [Online]. Available: https://www.everythingrf.com/News/details/8020-SAW-Device-Market-to-Grow-to-US-3-4-Billion-by-2024

[10] Y.-Q. Lu, Y.-Y. Zhu, Y.-F. Chen, S.-N. Zhu, N.-B. Ming, and Y.-J. Feng, "Optical properties of an ionic-type phononic crystal," *Science*, vol. 284, no. 5421, pp. 1822–1824, 1999. doi: 10.1126/science.284.5421.1822.

[11] Y-y. Zhu, X-j. Zhang, Y-q. Lu, Y-f. Chen, S-n. Zhu, and N-b. Ming, "New type of polariton in a piezoelectric superlattice," *Phys. Rev. Lett.*, vol. 90, no. 5, p. 053903, 2003. doi: 10.1103/PhysRevLett.90.053903.

[12] C-p. Huang and Y-y. Zhu, "Piezoelectric-induced polariton coupling in a superlattice," *Phys. Rev. Lett.*, vol. 94, no. 11, p. 117,401, 2005. doi: 10.1103/PhysRevLett.94.117401.

[13] R.-C. Yin, C. He, M.-H. Lu, Y.-Q. Lu, and Y.-F. Chen, "Polaritons in an artificial ionic-type crystal made of two-dimensional periodically inversed multi-domain ferroelectric crystals," *J. Appl. Phys.*, vol. 109, no. 6, p. 064110, 2011. doi: 10.1063/1.3554831.

[14] D. Yudistira, A. Boes, D. Janner, V. Pruneri, J. Friend, and A. Mitchell, "Polariton-based band gap and generation of surface acoustic waves in acoustic superlattice lithium niobate," *J. Appl. Phys.*, vol. 114, no. 5, p. 054904, 2013. doi: 10.1063/1.4817271.

[15] D. Yudistira et al., "Monolithic phononic crystals with a surface acoustic band gap from surface phonon-polariton coupling," *Phys. Rev. Lett.*, vol. 113, no. 21, p. 215,503, 2014. doi: 10.1103/PhysRevLett.113.215503.

[16] R. W. Whatmore, P. A. Goddard, B. K. Tanner, and G. F. Clark, "Direct imaging of travelling Rayleigh waves by stroboscopic X-ray topography," *Nature*, vol. 299, no. 5878, pp. 44–46, 1982. doi: 10.1038/299044a0.

[17] E. Zolotoyabko, D. Shilo, W. Sauer, E. Pernot, and J. Baruchel, "Visualization of 10 μm surface acoustic waves by stroboscopic x-ray topography," *Appl. Phys. Lett.*, vol. 73, no. 16, pp. 2278–2280, 1998. doi: 10.1063/1.121701.

[18] W. Sauer et al., "X-ray imaging and diffraction from surface phonons on GaAs," *Appl. Phys. Lett.*, vol. 75, pp. 1709–1711, 1999. doi: 10.1063/1.124797.

[19] A. Mahjoubfar, K. Goda, A. Ayazi, A. Fard, S. H. Kim, and B. Jalali, "High-speed nanometer-resolved imaging vibrometer and velocimeter," *Appl. Phys. Lett.*, vol. 98, no. 10, p. 101,107, 2011. doi: 10.1063/1.3563707.

[20] Y. Xu, W. Fu, C-l. Zou, Z. Shen, and H. X. Tang, "High quality factor surface Fabry–Perot cavity of acoustic waves," *Appl. Phys. Lett.*, vol. 112, no. 7, p. 073505, 2018. doi: 10.1063/1.5013161.

[21] Y. Sugawara et al., "Watching ripples on crystals," *Phys. Rev. Lett.*, vol. 88, no. 18, p. 185,504, 2002. doi: 10.1103/PhysRevLett.88.185504.

[22] D. M. Profunser, O. B. Wright, and O. Matsuda, "Imaging ripples on phononic crystals reveals acoustic band structure and Bloch harmonics," *Phys. Rev. Lett.*, vol. 97, no. 5, p. 055502, 2006. doi: 10.1103/PhysRevLett.97.055502.

[23] O. B. Wright and O. Matsuda, "Watching surface waves in phononic crystals," *Phil. Trans. R. Soc. A*, vol. 373, no. 2049, p. 20,140,364, 2015. doi: 10.1098/rsta.2014.0364.

[24] D. V. Roshchupkin, T. Fournier, M. Brunel, O. A. Plotitsyna, and N. G. Sorokin, "Scanning electron microscopy observation of excitation of the surface acoustic waves by the regular domain structures in the $LiNbO_3$ crystals," *Appl. Phys. Lett.*, vol. 60, no. 19, pp. 2330–2331, 1992. doi: 10.1063/1.107016.

[25] D. V. Roshchupkin, M. Brunel, R. Tucoulou, E. Bigler, and N. G. Sorokin, "Reflection of surface acoustic waves on domain walls in a $LiNbO_3$ crystal," *Appl. Phys. Lett.*, vol. 64, no. 2, pp. 164–165, 1994. doi: 10.1063/1.111552.

[26] D. V. Roshchupkin and M. Brunel, "Scanning electron microscopy observation of surface acoustic wave propagation in the $LiNbO_3$ crystals with regular domain structures," *IEEE Trans. Ultrason. Ferroelectr. Freq. Control*, vol. 41, no. 4, pp. 512–517, 1994. doi: 10.1109/58.294112.

[27] T. Hesjedal and G. Behme, "High-resolution imaging of surface acoustic wave scattering," *Appl. Phys. Lett.*, vol. 78, no. 13, p. 1948, 2001. doi: 10.1063/1.1357453.

[28] T. Hesjedal and G. Behme, "AFM observation of surface acoustic waves emitted from single symmetric SAW transducers," *IEEE Trans. Ultrason. Ferroelectr. Freq. Control Lett.*, vol. 48, no. 3, p. 641, 2001. doi: 10.1109/58.920685.

[29] G. Behme and T. Hesjedal, "Influence of surface acoustic waves on lateral forces in scanning force microscopies," *J. Appl. Phys.*, vol. 89, no. 9, p. 4850, 2001. doi: 10.1063/1.1362413.

[30] T. Hesjedal and G. Behme, "High-resolution imaging of a single circular surface acoustic wave source: Effects of crystal anisotropy," *Appl. Phys. Lett.*, vol. 79, no. 7, pp. 1054–1056, 2001. doi: 10.1063/1.1394170.

[31] T. Hesjedal, "Surface acoustic wave-assisted scanning probe microscopy: A summary," *Rep. Prog. Phys.*, vol. 73, no. 1, p. 016102, 2010. doi: 10.1088/0034-4885/73/1/016102.

[32] I. Yahyaie, D. A. Buchanan, G. E. Bridges, D. J. Thomson, and D. R. Oliver, "High-resolution imaging of gigahertz polarization response arising from the interference of reflected surface acoustic waves," *IEEE Trans. Ultrason. Ferroelect. Freq. Control*, vol. 59, no. 6, pp. 1212–1218, June 2012.

[33] K. Takata, T. Hasegawa, S. Hosaka, S. Hosoki, and T. Komoda, "Tunneling acoustic microscope," *Appl. Phys. Lett.*, vol. 55, no. 17, p. 1718, 1989. doi: 10.1063/1.102199.

[34] W. Rohrbeck, E. Chilla, H.-J. Fröhlich, and J. Riedel, "Detection of surface acoustic waves by scanning tunneling microscopy," *Appl. Phys. A*, vol. 52, no. 5, p. 344, 1991. doi: 10.1007/BF00324777.

[35] E. Chilla, W. Rohrbeck, H.-J. Fröhlich, R. Koch, and K. H. Rieder, "Probing of surface acoustic wave fields by a novel scanning tunneling microscopy technique: Effects of topography," *Appl. Phys. Lett.*, vol. 61, no. 26, p. 3107, 1992. doi: 10.1063/1.108478.

[36] T. Hesjedal, E. Chilla, and H.-J. Fröhlich, "Direct visualization of the oscillation of Au (111) surface atoms," *Appl. Phys. Lett.*, vol. 69, no. 3, p. 354, 1996. doi: 10.1063/1.118058.

[37] B. A. Richardson and G. S. Kino, "Probing of elastic surface waves in piezoelectric media," *Appl. Phys. Lett.*, vol. 16, no. 2, p. 82, 1970. doi: 10.1063/1.1653109.

Authorized licensed use limited to: Cornell University Library. Downloaded on September 08,2020 at 12:56:23 UTC from IEEE Xplore. Restrictions apply.

[38] Y. L. Yang et al., "Batch-fabricated cantilever probes with electrical shielding for nanoscale dielectric and conductivity imaging," *J. Micromech. Microeng.*, vol. 22, no. 11, p. 115,040, 2012. doi: 10.1088/0960-1317/22/11/115040.

[39] K. Lai, W. Kundhikanjana, M. Kelly, and Z. X. Shen, "Modeling and characterization of a cantilever-based near-field scanning microwave impedance microscope," *Rev. Sci. Instrum.*, vol. 79, no. 6, p. 063703, 2008. doi: 10.1063/1.2949109.

[40] K. Lai, W. Kundhikanjana, M. Kelly, and Z. X. Shen, "Nanoscale microwave microscopy using shielded cantilever probes," *Appl. Nanosci.*, vol. 1, no. 1, pp. 13–18, 2011. doi: 10.1007/s13204-011-0002-7.

[41] L. Zheng, D. Wu, X. Wu, and K. Lai, "Visualization of surface-acoustic-wave potential by transmission-mode microwave impedance microscopy," *Phys. Rev. Appl.*, vol. 9, p. 061002, June 2018.

[42] A. S. Thanawalla et al., "Microwave near-field imaging of electric fields in a superconducting microstrip resonator," *Appl. Phys. Lett.*, vol. 73, no. 17, p. 2491, 1998. doi: 10.1063/1.122492.

[43] S. K. Dutta et al., "Imaging microwave electric fields using a near-field scanning microwave microscope," *Appl. Phys. Lett.*, vol. 74, no. 1, p. 156, 1999. doi: 10.1063/1.123137.

[44] K. Lai, T. Ma, X. Bo, S. Anlage, and G. Shvets, "Experimental realization of a reflections-free compact delay line based on a photonic topological insulator," *Sci. Rep.*, vol. 6, p. 28,453, June 2016.

[45] F. Gao et al., "Topologically protected refraction of robust kink states in valley photonic crystals," *Nature Phys.*, vol. 14, no. 2, pp. 140–144, 2018. doi: 10.1038/nphys4304.

[46] R. S. Weis and T. K. Gaylord, "Lithium niobate: Summary of physical properties and crystal structure," *Appl. Phys. A*, vol. 37, no. 4, pp. 191–203, 1985. doi: 10.1007/BF00614817.

[47] J. Slobodnik, Jr., P. H. Carr, and A. J. Budreau, "Microwave frequency acoustic surface-wave loss mechanisms on LiNbO$_3$," *J. Appl. Phys.*, vol. 41, no. 11, p. 4380, 1970. doi: 10.1063/1.1658471.

[48] K. Yamanouchi and K. Shibayama, "Propagation and amplification of rayleigh waves and piezoelectric leaky surface waves in LiNbO$_3$," *J. Appl. Phys.*, vol. 43, no. 3, p. 856, 1972. doi: 10.1063/1.1661294.

[49] M. Yamada, N. Nada, M. Saitoh, and K. Watanabe, "First-order quasi-phase matched LiNbO$_3$ waveguide periodically poled by applying an external field for efficient blue second-harmonic generation," *Appl. Phys. Lett.*, vol. 62, no. 5, p. 435–436, 1993. doi: 10.1063/1.108925.

[50] H. Liang, R. Luo, Y. He, H. Jiang, and Q. Lin, "High-quality lithium niobate photonic crystal nanocavities," *Optica*, vol. 4, no. 10, p. 1251–1258, 2017. doi: 10.1364/OPTICA.4.001251.

[51] L. Zheng et al., "Interferometric imaging of nonlocal electromechanical power transduction in ferroelectric domains," *Proc. Natl. Acad. Sci.*, vol. 115, no. 21, pp. 5338–5342, 2018. doi: 10.1073/pnas.1722499115.

[52] S. R. Johnston et al., "Measurement of surface acoustic wave resonances in ferroelectric domains by microwave microscopy," *J. Appl. Phys.*, vol. 122, no. 7, p. 074101, 2017. doi: 10.1063/1.4997474.

[53] A. Takayanagi, K. Yamanouchi, and K. Shibayama, "Piezoelectric leaky surface wave in LiNbO$_3$," *Appl. Phys. Lett.*, vol. 17, no. 5, pp. 225–227, 1970. doi: 10.1063/1.1653375.

[54] D. Royer and E. Dieulesaint, *Elastic Waves in Solids*. Berlin: Springer-Verlag, 1999.

[55] J. L. Bleustein, "A new surface wave in piezoelectric materials," *Appl. Phys. Lett.*, vol. 13, no. 12, pp. 412–413, 1968. doi: 10.1063/1.1652495.

[56] Y. V. Gulyaev, "Electroacoustic surface waves in piezoelectric materials," *JETP Lett.*, vol. 9, p. 37, 1969.

[57] R. M. White, "Surface elastic waves," *Proc. IEEE*, vol. 58, no. 8, pp. 1238–1276, 1970. doi: 10.1109/PROC.1970.7900.

[58] M. F. Crommie, C. P. Lutz, and D. M. Eigler, "Confinement of electrons to quantum corrals on a metal surface," *Science*, vol. 262, no. 5131, pp. 218–220, 1993. doi: 10.1126/science.262.5131.218.

[59] S. Fujii et al., "Low propagation loss in a one-port SAW resonator fabricated on single-crystal diamond for super-high-frequency applications," *IEEE Trans. Ultrason. Ferroelect. Freq. Control*, vol. 60, no. 5, pp. 986–992, 2013. doi: 10.1109/TUFFC.2013.2656.

[60] R. Manenti, M. J. Peterer, A. Nersisyan, E. B. Magnusson, A. Patterson, and P. J. Leek, "Surface acoustic wave resonators in the quantum regime," *Phys. Rev. B*, vol. 93, no. 4, p. 041411(R), 2016. doi: 10.1103/PhysRevB.93.041411.

[61] L. Shao et al., "Phononic band structure engineering for high-Q gigahertz surface acoustic wave resonators on lithium niobate," *Phys. Rev. Appl.*, vol. 12, p. 014022, July 2019.

[62] D. Wu et al., "Thickness-dependent dielectric constant of few-layer In$_2$Se$_3$ nanoflakes," *Nano Lett.*, vol. 15, no. 12, pp. 8136–8140, 2015. doi: 10.1021/acs.nanolett.5b03575.

[63] X. Wu et al., "Low-energy structural dynamics of ferroelectric domain walls in hexagonal rare-earth manganites," *Sci. Adv.*, vol. 3, no. 5, p. e1602371, 2017. doi: 10.1126/sciadv.1602371.

[64] D. Wu et al., "Uncovering edge states and electrical inhomogeneity in MoS$_2$ field-effect transistors," *Proc. Natl. Acad. Sci.*, vol. 113, no. 31, pp. 8583–8588, 2016. doi: 10.1073/pnas.1605982113.

[65] Y. Chu et al., "Quantum acoustics with superconducting qubits," *Science*, vol. 358, no. 6360, pp. 199–202, 2017. doi: 10.1126/science.aao1511.

[66] M. Kervinen, I. Rissanen, and M. Sillanpää, "Interfacing planar superconducting qubits with high overtone bulk acoustic phonons," *Phys. Rev. B*, vol. 97, no. 20, p. 205,443, 2018. doi: 10.1103/PhysRevB.97.205443.

[67] P. Arrangoiz-Arriola et al., "Coupling a superconducting quantum circuit to a phononic crystal defect cavity," *Phys. Rev. X*, vol. 8, no. 3, p. 031007, 2018. doi: 10.1103/PhysRevX.8.031007.

[68] M. J. A. Schuetz, E. M. Kessler, G. Giedke, L. M. K. Vandersypen, M. D. Lukin, and J. I. Cirac, "Universal quantum transducers based on surface acoustic waves," *Phys. Rev. X*, vol. 5, no. 3, p. 031031, 2015. doi: 10.1103/PhysRevX.5.031031.

[69] D. A. Golter, T. Oo, M. Amezcua, K. A. Stewart, and H. Wang, "Optomechanical quantum control of a nitrogen-vacancy center in diamond," *Phys. Rev. Lett.*, vol. 116, no. 14, p. 143,602, 2016. doi: 10.1103/PhysRevLett.116.143602.

[70] S. J. Whiteley et al., "Spin–phonon interactions in silicon carbide addressed by Gaussian acoustics," *Nat. Phys.*, vol. 15, no. 5, pp. 490–495, 2019. doi: 10.1038/s41567-019-0420-0.

[71] S. A. Tadesse and M. Li, "Sub-optical wavelength acoustic wave modulation of integrated photonic resonators at microwave frequencies," *Nat. Commun.*, vol. 5, pp. 5402, Nov. 2014. doi: 10.1038/ncomms6402.

[72] S. Kapfinger et al., "Dynamic acousto-optic control of a strongly coupled photonic molecule," *Nat. Commun.*, vol. 6, pp. 1–6, Oct. 2015 Art. no. 8540.

[73] K. Fang, M. H. Matheny, X. Luan, and O. Painter, "Optical transduction and routing of microwave phonons in cavity-optomechanical circuits," *Nat. Photon.*, vol. 10, no. 7, p. 489–496, 2016. doi: 10.1038/nphoton.2016.107.

[74] S. Hermelin et al., "Electrons surfing on a sound wave as a platform for quantum optics with flying electrons," *Nature*, vol. 477, no. 7365, pp. 435–438, 2011. doi: 10.1038/nature10416.

[75] R. P. G. McNeil et al., "On-demand single-electron transfer between distant quantum dots," *Nature*, vol. 477, no. 7365, pp. 439–442, 2011. doi: 10.1038/nature10444.

[76] M. J. A. Schuetz, J. Knörzer, G. Giedke, L. M. K. Vandersypen, M. D. Lukin, and J. I. Cirac, "Acoustic traps and lattices for electrons in semiconductors," *Phys. Rev. X*, vol. 7, no. 4, p. 041019, 2017. doi: 10.1103/PhysRevX.7.041019.

[77] L. Shao et al., "Microwave-to-optical conversion using lithium niobate thin-film acoustic resonators," *Optica*, vol. 6, no. 12, pp. 1498–1505, 2019. doi: 10.1364/OPTICA.6.001498.

[78] S. Maity et al., "Coherent acoustic control of a single silicon vacancy spin in diamond," *Nature Commun.*, vol. 11, p. 193, Jan. 2020.

[79] P. Wang, L. Lu, and K. Bertoldi, "Topological phononic crystals with one-way elastic edge waves," *Phys. Rev. Lett.*, vol. 115, no. 10, p. 104302, 2015. doi: 10.1103/PhysRevLett.115.104302.

[80] K. Lai, W. Kundhikanjana, J. Shabani, M. Shayegan, M. A. Kelly, and Z.-X. Shen, "Imaging of the Coulomb driven quantum Hall edge states," *Phys. Rev. Lett.*, vol. 107, no. 17, p. 176809, 2011. doi: 10.1103/PhysRevLett.107.176809.

[81] E. Y. Ma et al., "Unexpected edge conduction in mercury telluride quantum wells under broken time-reversal symmetry," *Nat. Commun.*, vol. 6, p. 7252, May 2015. doi: 10.1038/ncomms8252.

Authorized licensed use limited to: Cornell University Library. Downloaded on September 08,2020 at 12:56:23 UTC from IEEE Xplore. Restrictions apply.